Supplementary

S1. Extended Experimental and Characterization Details

S1.1. Materials and Instrumental Parameters

All chemical reagents used in this study, including $SbCl_3$ (99.95%) and HCl (38%), were purchased from commercial sources and used without further purification. The organic precursor $C_8H_{12}N_2$ was employed as received. The compound $(C_8H_{14}N_2)[SbCl_5]$ was prepared according to the synthetic procedure described in the main text. The following instruments and settings were employed for the different characterizations:

Optical analyses: Diffuse reflectance spectra (DRS) were recorded in the solid phase using a PerkinElmer Lambda 35 UV–Vis spectrophotometer equipped with an integrating sphere, over the spectral range of 200–1100 nm. Samples were prepared as compressed pellets of 6 mm diameter to ensure high optical density and uniform reflectivity. The reflectance data were converted to absorption using the Kubelka–Munk function for band gap analysis.

Photoluminescence (PL): The PL emission spectra were acquired at room temperature using a PerkinElmer LS 55 fluorescence spectrometer with a 150 W xenon lamp as excitation source. The excitation wavelength was selected based on the main absorption edge observed in the UV–Vis spectra, and the emission was collected with a 0.5 nm step size to ensure spectral precision.

Electrical impedance measurements: The electrical and dielectric properties were measured using a Solartron SI 1260 impedance/gain-phase analyzer operating within the frequency range 40–10^7 Hz and temperature range 40–140 K. The sample pellets (1 mm thick, 6 mm diameter) were sandwiched between gold electrodes to ensure ohmic contact. Temperature control was achieved with a precision of ±0.1 K using a closed-cycle helium cryostat.

All data acquisition and treatment were performed with the ZView and Origin software packages. The detailed calibration procedures, background corrections, and instrumental configurations are available upon request.

S1.2. Complementary Synthesis and Structural Characterization

Following the synthetic route described in the main text, slow evaporation of the aqueous solution containing the organic precursor ($C_8H_{12}N_2$), $SbCl_3$, and concentrated HCl (38%) led to the formation of colorless, prism-shaped crystals after four days of equilibration under ambient conditions. The crystalline product was filtered, air-dried, and stored in a desiccator prior to use.

The crystallographic analysis of the compound confirmed that it crystallizes in the monoclinic system with the P 2_1/n space group, consistent with the previously reported structure **(CCDC 2382366)**. This structural identity ensures reproducibility and structural consistency between batches. The detailed synthesis parameters, such as solvent volume, reagent ratios, and reaction time, were optimized to promote the growth of single crystals suitable for X-ray diffraction.

To verify the compositional purity and homogeneity of the synthesized compound, energy-dispersive X-ray spectroscopy (EDS) coupled with elemental mapping was performed (Fig. 1.S). The EDS spectrum, acquired at 20 kV and 1000× magnification, exhibits only the characteristic peaks of nitrogen, chlorine, and antimony, confirming the exclusive presence of the expected elements. The corresponding elemental maps demonstrate the uniform spatial distribution of Sb and Cl across the crystalline domains, with nitrogen homogeneously incorporated throughout the lattice. As expected, hydrogen is not detected due to its very low atomic number, while the carbon signal remains weak and often obscured in EDS due to surface contamination and limited sensitivity. The absence of any extraneous peaks verifies the high chemical purity and compositional stability of the synthesized hybrid material.

Complementary powder X-ray diffraction (PXRD) analysis was performed to further confirm phase purity (Fig. 2.S). The experimental diffraction pattern (red curve) exhibits sharp, intense reflections indicative of excellent crystallinity and perfectly matches the simulated pattern (black curve) generated from the single-crystal X-ray diffraction data. The concordance of peak positions and intensities confirms that the bulk product is phase-pure and free from secondary crystalline impurities. This structural correlation validates the successful synthesis of a single-phase antimony–chloride hybrid framework.

A photograph of a representative single crystal of $(C_8H_{14}N_2)[SbCl_5]$ used for the structural study is provided in Fig. 3.S, highlighting the transparent and well-faceted nature of the obtained crystals. The image provides a visual confirmation of the high quality and macroscopic uniformity of the crystal specimens.

S1.3. Computational Details

The theoretical calculations were performed using the Gaussian 09W software package. The DFT and TD-DFT computations employed the hybrid B3LYP functional in conjunction with the LanL2DZ basis set. The model system consisted of one $(C_8H_{14}N_2)^{2+}$ cation and one $[SbCl_5]^{2-}$ anion, representing a single molecular unit extracted from the crystal structure. Full geometry optimization was conducted with tight convergence criteria (energy threshold 10^{-6} a.u., maximum

force < 0.00045 a.u.), and frequency calculations confirmed the absence of imaginary modes, ensuring a true energy minimum.

Electronic absorption properties were investigated through TD-DFT simulations to evaluate the nature of the optical transitions. The HOMO–LUMO energy levels and frontier orbital distributions were visualized using GaussView 6.0.16. The molecular electrostatic potential (MEP) and electronic density distributions were analyzed using the Multiwfn 3.8 program [27]. These theoretical analyses were performed to support the experimental findings and provide deeper insight into the charge-transfer processes within the hybrid system.

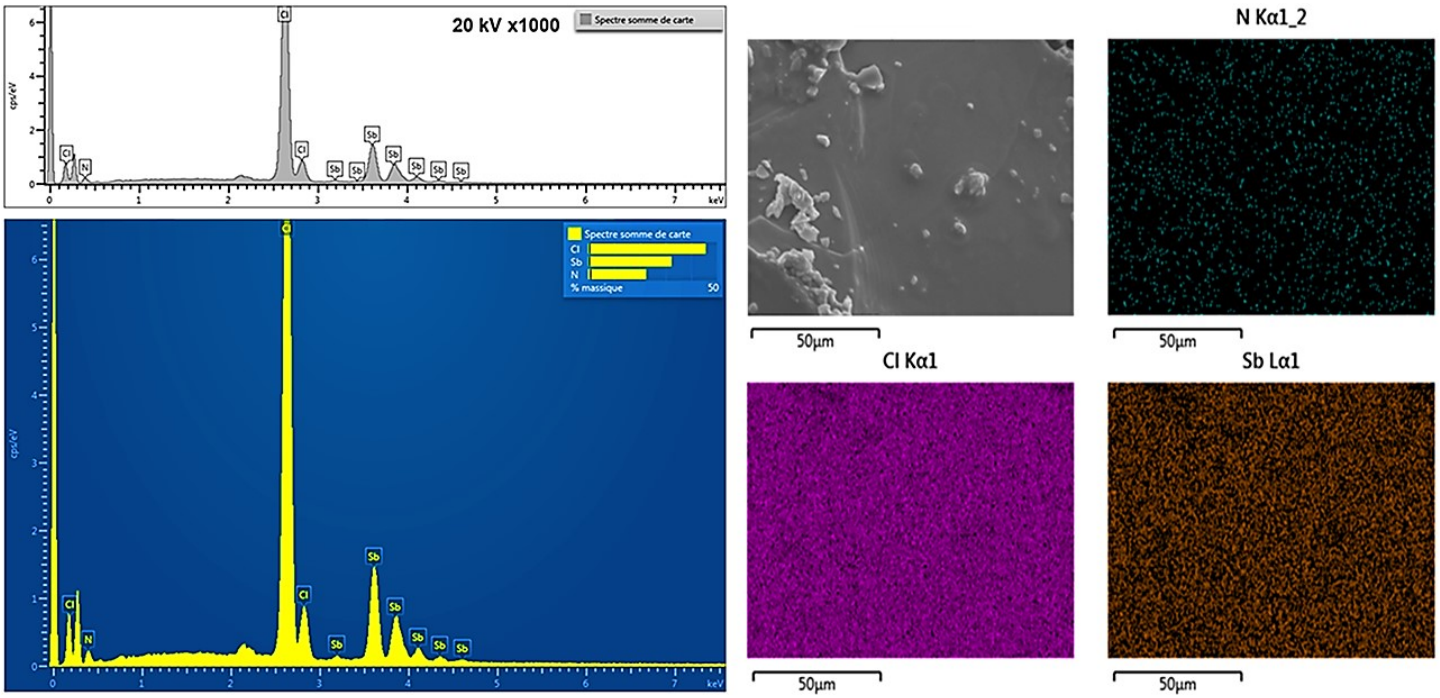

Fig. 1.S: EDS spectrum and elemental mapping of $(C_8H_{14}N_2)[SbCl_5]$

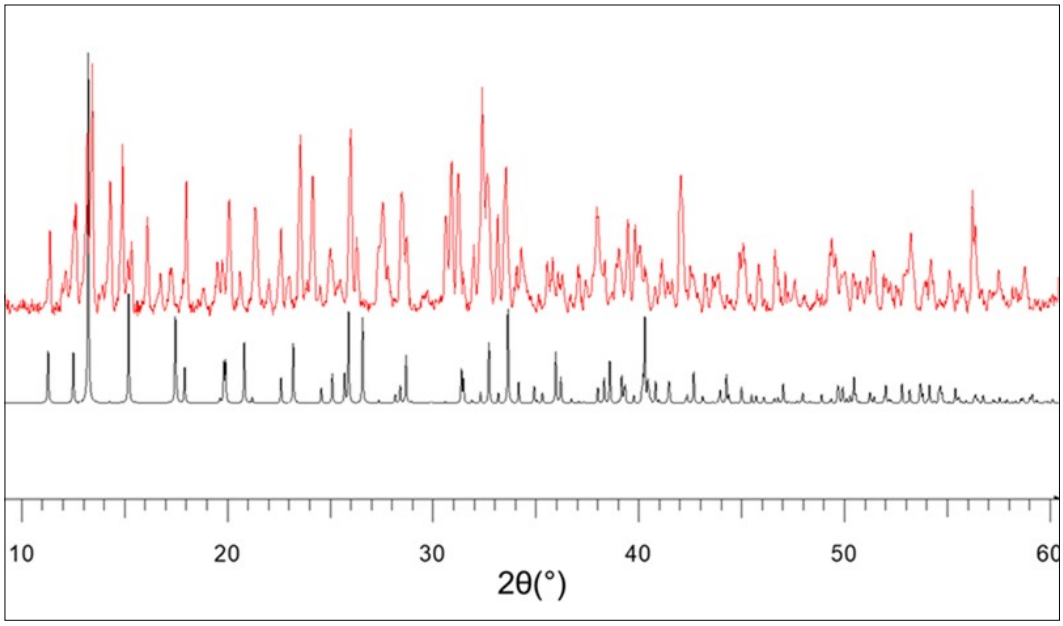

Fig. *2*.S: PXRD pattern with experimental (red) and simulated (black) data

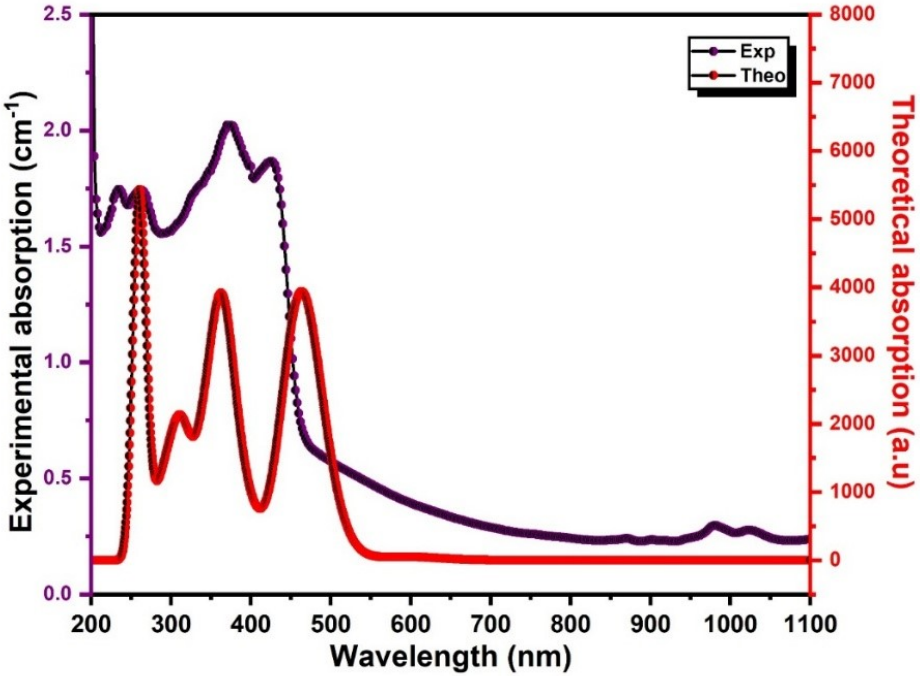

Fig. 3.S: Comparative Analysis of DFT and Experimental Absorption Profiles

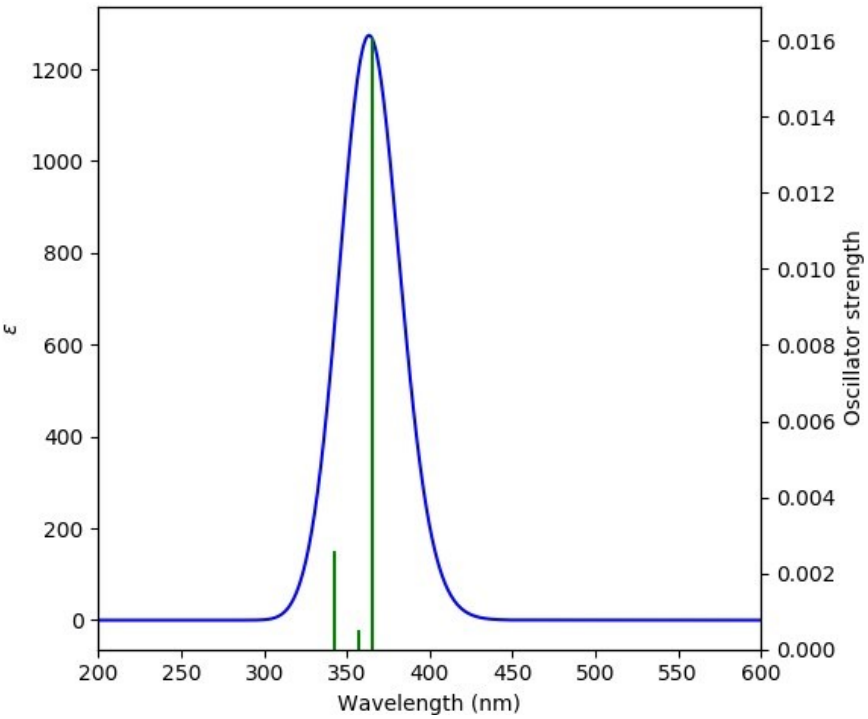

Fig. .S: Simulated UV-Visible spectrum.

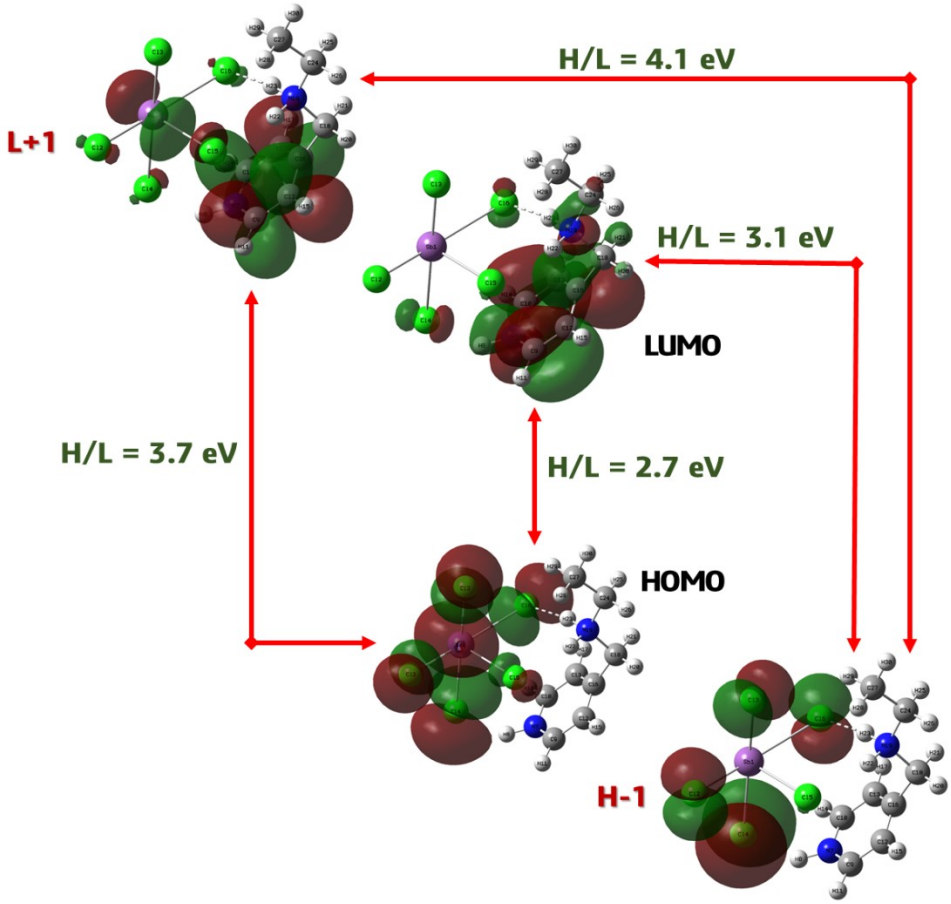

Fig. 5.S: The selected MO drawings for the compound.

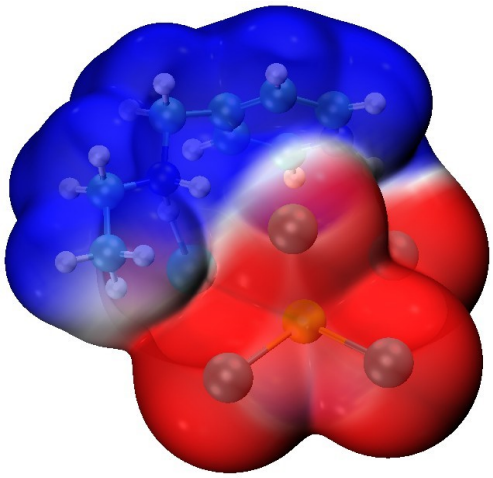

Fig. 6.S: Molecular Electrostatic Potential (MEP) Map of $(C_8H_{14}N_2)[SbCl_5]$

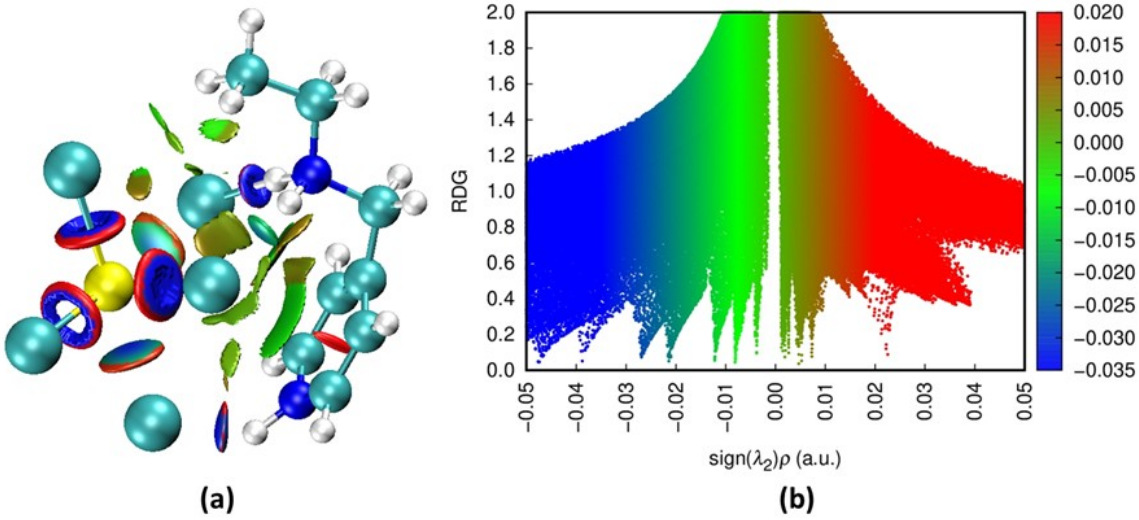

Fig. 7.S: Non-Covalent Interaction (NCI-RDG) Analysis of $(C_8H_{14}N_2)[SbCl_5]$

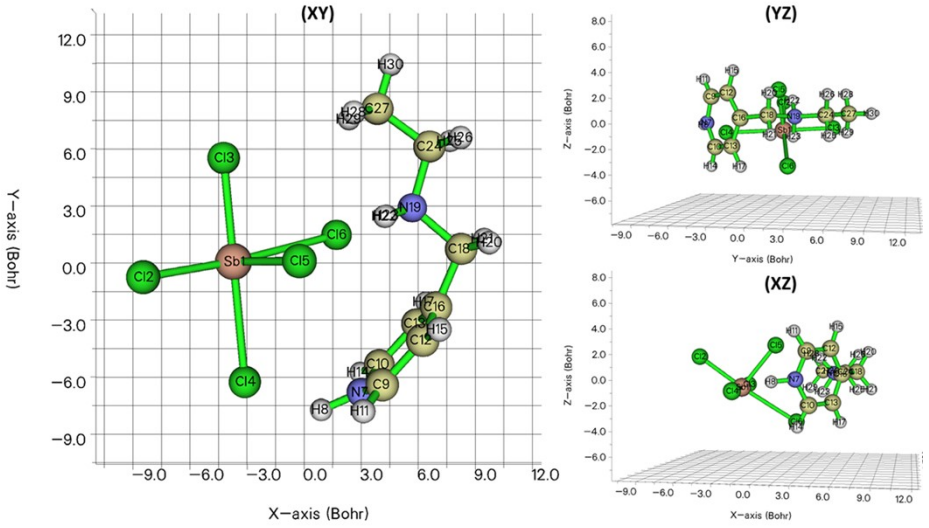

Fig. 8.S: Theoretical Structural Representation of $(C_8H_{14}N_2)[SbCl_5]$ in the (XY), (XZ), and (YZ) Planes

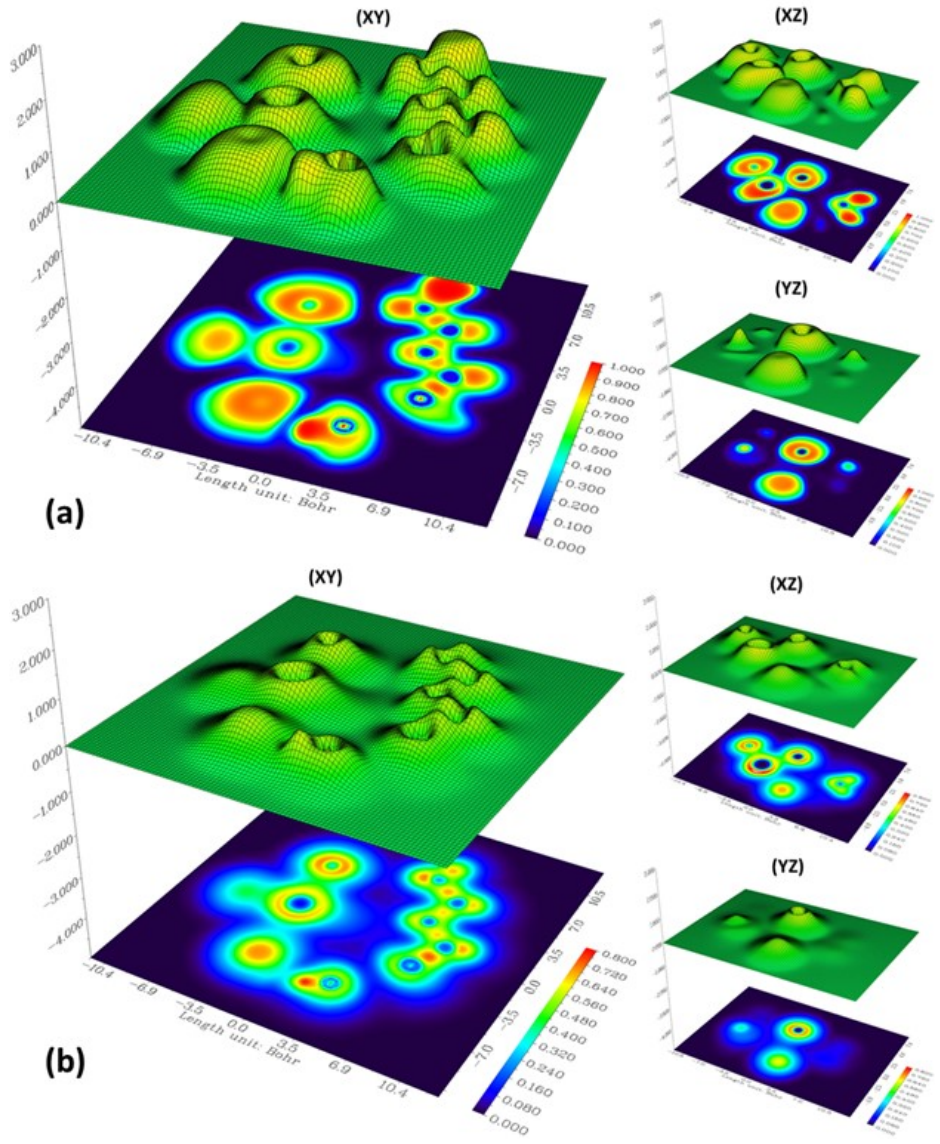

Fig. 9.S: (a) Electron Localization Function (ELF) and **(b)** Localized Orbital Locator (LOL) Analysis of $(C_8H_{14}N_2)[SbCl_5]$

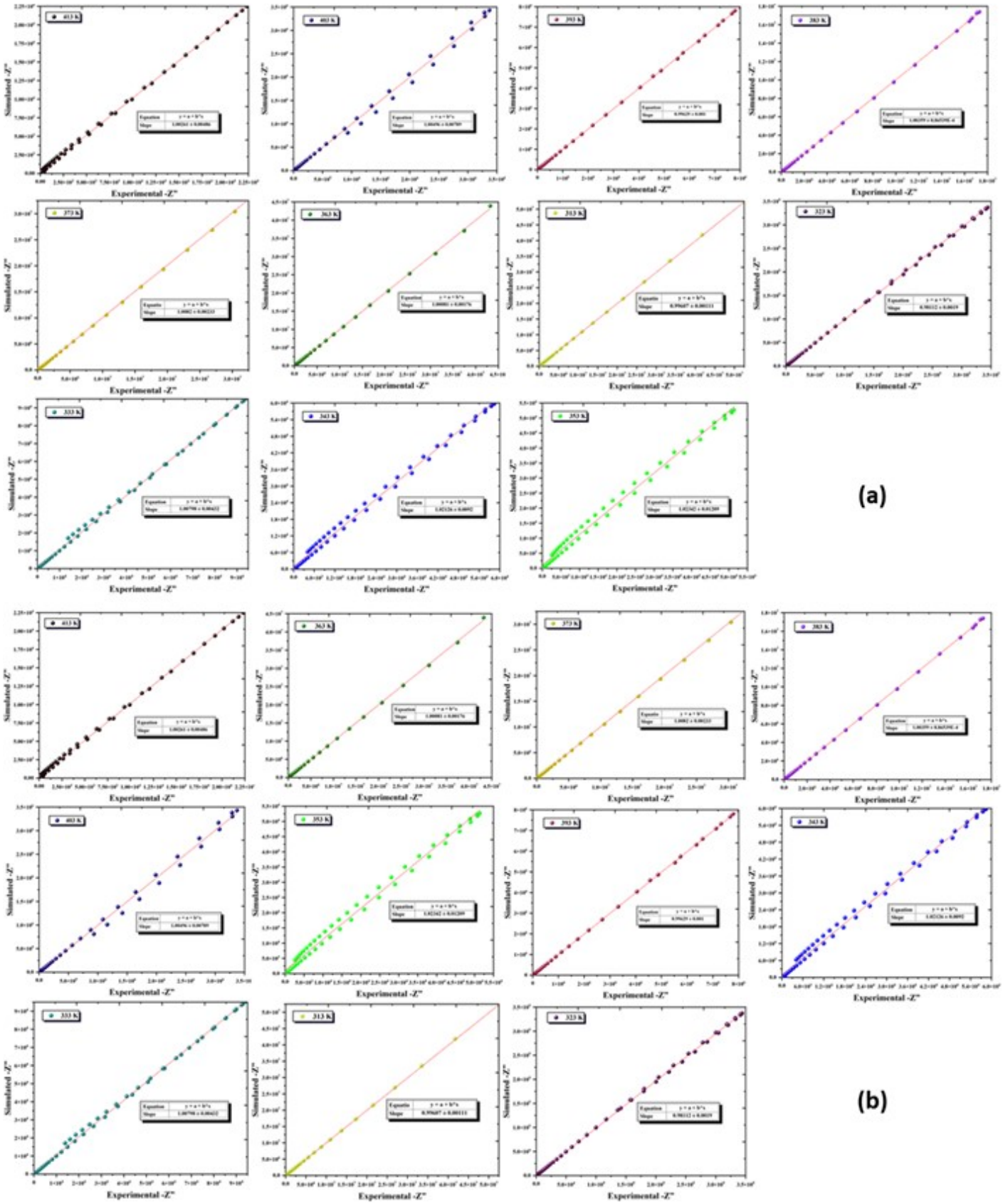

Fig. 10.S: Comparison of Measured and Simulated Impedance Values (**(a):** Z' (experimental) vs Z' (simulated) and **(b):** Z'' (experimental) vs Z'' (simulated))

Table 1.S: Calculated global reactivity parameters of the new compound.

Parameter	Value (eV)
HOMO	**-6.32**
LUMO	**-3.62**
E_A	**3.62**
E_I	**6.32**
μ	**-4.97**
η	**1.35**
S	**0.37**
ω	**9.15**
χ	**4.97**

Table 2.S: The calculated wavelengths, oscillator strengths, and major contributions for electronic transitions.

Wavelength (nm)	Oscillator strength	Major contribution
365.1749	0.0161	HOMO → LUMO (97%)
356.7890	0.0005	H-1 → LUMO (95%), H-1 → L+1 (3%)
342.6302	0.0026	HOMO → L+1 (98%)